

Minimally Entangled Typical Thermal States Algorithms for Finite Temperature Matsubara Green Functions.

Daniel Bauernfeind,¹ Xiaodong Cao,^{1,*} E. Miles Stoudenmire,¹ and Olivier Parcollet^{1,2}

¹*Center for Computational Quantum Physics, Flatiron Institute, 162 5th Avenue, New York, NY 10010, USA*

²*Université Paris-Saclay, CNRS, CEA, Institut de Physique Théorique, 91191, Gif-sur-Yvette, France*

(Dated: July 30, 2021)

We extend finite-temperature tensor network methods to compute Matsubara imaginary-time correlation functions, building on the minimally entangled typical thermal states (METTS) and purification algorithms. While imaginary-time correlation functions are straightforward to formulate with these methods, care is needed to avoid convergence issues that would result from naive estimators. As a benchmark, we study the single-band Anderson impurity model, even though the algorithm is quite general and applies to lattice models. The special structure of the impurity model benchmark system and our choice of basis enable techniques such as reuse of high-probability METTS for increasing algorithm efficiency. The results are competitive with state-of-the-art continuous time Monte Carlo. We discuss the behavior of computation time and error as a function of the number of purified sites in the Hamiltonian.

I. INTRODUCTION

The development of high precision quantum many-body physics is a rapidly growing field, whose purpose is to obtain controlled solutions of strongly interacting quantum systems. One direction of research are tensor network methods, which represent ground state many-body wavefunctions through a low-rank tensor decomposition. The first and most famous approach of this class is the density matrix renormalization group (DMRG) [1–3] which is very efficient for one dimensional systems and whose modern form is now understood in terms of matrix-product state (MPS) tensor networks.

The computation of real time dynamics and correlators in DMRG and tensor methods has been studied extensively, for a review see e.g. Ref. 4. However, in order to study the thermodynamics and much of the equilibrium properties of a system, the complete and detailed knowledge of real time dynamics is not necessary. The Matsubara *imaginary time* formalism in thermal equilibrium is sufficient and is almost always easier computationally since imaginary time evolution involves decaying exponentials. Indeed, many physical properties of a system can be derived from Matsubara self-energy, such as the Fermi liquid effective mass, quasiparticle lifetime, or the location of the Fermi surface. Real frequency correlators can also be obtained to some extent at low energy from imaginary time results by using analytical continuation techniques, for example Padé approximants.

Quantum Monte Carlo (QMC) methods typically work in Matsubara imaginary time (with some notable recent exceptions [5–9]). However they face limitations within some parameter ranges, especially at low temperatures. The most famous is the sign problem, which affects most QMC methods and manifests itself as an exponential increase of error bars at low temperatures.

Certain other QMC methods such as diagrammatic QMC [10], which computes perturbative series with stochastic techniques, face difficulties with convergence as the interaction strength is increased, see e.g. Ref. 8. It is therefore very interesting to explore the computation of Matsubara Green functions at finite temperature using tensor network methods for various systems, since these methods are not limited in the same way.

Apart from the imaginary time evolution itself, the main challenge in obtaining the Matsubara Green function is computing *finite temperature* versus ground state properties. Within tensor network methods, finite temperature systems can be accessed in two ways: (i) the minimally entangled typical thermal states (METTS) algorithm [11–15] uses a sampling technique over tensor network states to produce the thermal average; (ii) the purification technique [16–19] rewrites the thermal trace as a average in a pure state in a larger space, obtained by imaginary time evolution.

In this paper, we show how to combine the METTS and the purification idea to compute the finite temperature Matsubara Green function with these tensor network approaches at any temperature. As a first benchmark application, we use the single-site one-band Anderson quantum impurity model. Indeed, quantum impurity models are a very interesting application for this algorithm in the context of dynamical mean field theory (DMFT) [20]. DMFT and its extensions constitute a systematic approach to strongly correlated systems, not only for models but also in realistic computation [21]. The core of the technique consists in solving quantum impurity models, in self-consistently determined baths, at low temperatures. These models are still complex many-body problems, and require advanced algorithms to solve them, such as continuous time QMC [22–25] the numerical renormalization group (NRG) [26, 27], DMRG [28–36], and recently more general tensor network approaches [37]. Most MPS-based DMFT solvers have focused on real time evolution, with some notable exceptions [32, 34, 36] but still at zero tem-

* xcao@flatironinstitute.org

perature. The METTS/purification hybrid algorithm presented in this paper works at finite temperature.

This paper is structured as follows. In Sec. II we briefly introduce the original METTS algorithm as well as how to combine METTS and purification and define the estimator to sample imaginary time correlators. In Sec. III we benchmark the algorithm on the Anderson Impurity model and discuss the balance between the METTS and purification in details.

II. METTS FOR IMAGINARY TIME CORRELATION FUNCTIONS

A. The METTS algorithm

The METTS algorithm [11, 12] is a particular form of quantum Monte Carlo. It computes finite temperature thermal averages

$$\langle A \rangle = \frac{1}{\mathcal{Z}} \text{Tr}[e^{-\beta H} A] \quad (1)$$

where A is an observable, β the inverse temperature, H the Hamiltonian and \mathcal{Z} the partition function. It is based on the observation that (1) can be rewritten as:

$$\begin{aligned} \langle A \rangle &= \frac{1}{\mathcal{Z}} \text{Tr}[e^{-\beta H} A] \\ &= \frac{1}{\mathcal{Z}} \sum_i \langle i | e^{-\beta H/2} A e^{-\beta H/2} | i \rangle \\ &= \frac{1}{\mathcal{Z}} \sum_i P(i) \langle \phi_i | A | \phi_i \rangle \end{aligned} \quad (2)$$

where ϕ and P are defined by

$$\begin{aligned} |\phi_i\rangle &\equiv e^{-\beta H/2} |i\rangle / \sqrt{P(i)} \\ P(i) &\equiv \langle i | e^{-\beta H} | i \rangle \end{aligned} \quad (3)$$

The states $|\phi_i\rangle$ are non-orthogonal but normalized. When the $|i\rangle$ are chosen to be a basis of classical, or unentangled product states, the resulting $|\phi_i\rangle$ are called METTS. The METTS algorithm performs the full imaginary time evolution $e^{-\beta H/2} |i\rangle$ at each step and samples the basis states $|i\rangle$ with a Monte Carlo procedure. The algorithm starts with a state $|i\rangle$, time-evolves it in imaginary time up to $\beta/2$, then computes observables as expectation values of the $|\phi_i\rangle$ states. After that, a new basis state $|j\rangle$ is chosen with probability $p(i \rightarrow j) = |\langle j | \phi_i \rangle|^2$. The collapse into the new basis state $|j\rangle$ can be computed efficiently [12] by recursively collapsing one site at a time.¹ Additionally, it

is worth noting that within the METTS algorithm, the newly sampled state $|j\rangle$ is always accepted as detailed balance is satisfied [12].

The METTS states $|\phi_i\rangle$ are non-trivial entangled states, hence tensor networks, such as matrix product states, are used to represent these states during and after the time evolution process. Note however that the actual METTS algorithm presented above is independent of the choice of wavefunction representation and could be implemented using any representation that allows $|\phi_i\rangle$ to be computed efficiently.

B. Imaginary time correlation functions

The finite-temperature correlation function of two operators A and B in imaginary time for a system with Hamiltonian H is defined as (note the unusual sign convention for G_{AB} used in this paper):

$$\begin{aligned} G_{AB}(\tau) &= \langle T_\tau A(\tau) B \rangle \\ A(\tau) &= e^{\tau H} A e^{-\tau H} \\ T_\tau A(\tau) B &= \begin{cases} +A(\tau) B & \tau > 0 \\ \pm B A(\tau) & \tau < 0, \end{cases} \end{aligned} \quad (4)$$

where the \pm sign depends on whether the operators A and B are fermionic ($-$) or bosonic ($+$). Here we will be treating the fermionic case. Because of the cyclic invariance of the thermal trace, $G_{AB}(\tau)$ can be written in two ways:

$$\begin{aligned} G_{AB}(\tau) &= \langle A(\tau) B \rangle = \frac{1}{\mathcal{Z}} \sum_i P(i) \underbrace{\langle \phi_i | A(\tau) B | \phi_i \rangle}_{G_i^+(\tau)} \\ G_{AB}(\tau) &= \langle B A(\tau - \beta) \rangle = \frac{1}{\mathcal{Z}} \sum_i P(i) \underbrace{\langle \phi_i | B A(\tau - \beta) | \phi_i \rangle}_{G_i^-(\tau)} \end{aligned} \quad (5)$$

where we have also written out each of the thermal averages as averages over the METTS labeled by i . While the exact thermal expectation value of these two ways of writing $G_{AB}(\tau)$ is necessarily the same, the estimators $G_i^+(\tau)$ and $G_i^-(\tau)$ generally differ for each individual METTS. Note that this is true even if A and B respects a symmetry, because the METTS states $|\phi_i\rangle$ can break this symmetry. Using the explicit form of $|\phi_i\rangle$ from (3), we have

$$\begin{aligned} G_i^+(\tau) &= P(i) \langle i | e^{-(\beta/2-\tau)H} A e^{-\tau H} B e^{-\beta H/2} | i \rangle \\ G_i^-(\tau) &= P(i) \langle i | e^{-\beta H/2} B e^{-\tilde{\tau} H} A e^{-(\beta/2-\tilde{\tau})H} | i \rangle \end{aligned} \quad (6)$$

where $\tilde{\tau} = \beta - \tau$. For $\tau, \tilde{\tau} > \beta/2$ these expressions can become very large because of the positive exponentials. Therefore, we use the following *symmetric estimator* defined by:

$$G_i(\tau) \equiv \begin{cases} G_i^+(\tau) & \text{for } \tau < \beta/2 \\ G_i^-(\tau) & \text{for } \tau > \beta/2 \text{ } (\tilde{\tau} < \beta/2) \end{cases} \quad (7)$$

¹ Repeated use of the product rule of probabilities allows to decompose $|\langle j | \phi_i \rangle|^2 \equiv P(j_1, j_2 \dots j_N | \phi_i) = P(j_1 | \phi_i) P(j_2 | j_1, \phi_i) P(j_3 | j_1, j_2, \phi_i) \dots P(j_N | j_1 \dots j_{N-1}, \phi_i)$ proving that the local collapse is correct.

Moreover this symmetric estimator also allows to reuse partially time-evolved states already computed during the calculation of the METTS $|\phi_i\rangle$: if the METTS states and their normalization are kept during the computation, the time evolved states

$$e^{-(\beta/2-\tau)H} |i\rangle, \quad (8)$$

for $\tau < \beta/2$ require no extra computation.

The main drawback of the symmetric estimator Eq. (7) is to introduce a discontinuity at $\beta/2$ for any finite number of samples, since $G_i^+(\beta/2)$ and $G_i^-(\beta/2)$ are in general not equal. We will discuss that point further in Sec. III C 2 on a concrete example.

C. Hybrid METTS-Purification algorithm

The METTS algorithm presented above has two main drawbacks, which we will now address by mixing it with the purification technique [14, 15]. First we will introduce purification then review how a controlled algorithm can be formulated which is hybrid of purification and METTS.

1. Purification

Let us start with a simple reminder of the purification idea. For each physical (spinless) fermionic degree of freedom P_i at site i with two states $|0\rangle_{P_i}$ and $|1\rangle_{P_i}$, we take the tensor product with an auxiliary or “ancilla” degree of freedom A_i with two states $|0\rangle_{A_i}$ and $|1\rangle_{A_i}$ and define the maximally entangled state S_i as

$$|S_i\rangle \equiv \frac{1}{\sqrt{2}} (|0\rangle_{P_i} \otimes |1\rangle_{A_i} + |1\rangle_{P_i} \otimes |0\rangle_{A_i}) \quad (9)$$

such that

$$\text{Tr}_{A_i} |S_i\rangle \langle S_i| = \mathbb{1}_{P_i} \quad (10)$$

where P_i or A_i refer to physical and auxiliary degrees of freedom on site i respectively (Tr_{A_i} is the trace over the auxiliary degrees of freedom).

The density matrix can then be rewritten as

$$\begin{aligned} \rho &= \frac{1}{\mathcal{Z}} e^{-\beta H/2} \cdot \mathbb{1}_P \cdot e^{-\beta H/2} \\ &= \frac{1}{\mathcal{Z}} e^{-\beta H/2} \text{Tr}_A \bigotimes_i \left(|S_i\rangle \langle S_i| \right) e^{-\beta H/2} \\ &= \frac{1}{\mathcal{Z}} \text{Tr}_A \left[\underbrace{\left(e^{-\beta H/2} \otimes \mathbb{1}_A \right)}_{|\psi_\beta\rangle} |S\rangle \langle S| \left(e^{-\beta H/2} \otimes \mathbb{1}_A \right) \right] \\ &= \frac{1}{\mathcal{Z}} \text{Tr}_A |\psi_\beta\rangle \langle \psi_\beta|. \end{aligned} \quad (11)$$

where $|S\rangle \equiv \bigotimes_i |S_i\rangle$, Tr_A is the trace over auxiliary degrees of freedom and the subscript P , (resp. A) means that the

operator acts on the physical (resp. auxiliary) space. We also used $\mathbb{1}_P \equiv \bigotimes_i \mathbb{1}_{P_i}$ and (10). In other words, at the cost of doubling the dimension of the Hilbert space, the introduction of the ancilla states lets us rewrite the density matrix as partial trace of a pure state density matrix, which can be obtained from a time evolution from $|S\rangle$ using pure-state time evolution methods.

2. Hybrid algorithm

The purification technique has two main advantages over the original METTS algorithm.

First, although the METTS algorithm implemented with MPS is highly efficient at low temperature and scales similarly to DMRG, its sampling becomes less efficient at high temperatures compared to the purification approach.

Secondly, because METTS updates remain in a fixed quantum-number sector corresponding to the symmetries of the Hamiltonian, one cannot straightforwardly use quantum numbers to simulate the grand canonical ensemble efficiently [12, 13]. On the contrary, using purification, the maximally entangled state $|S\rangle$ allows particle numbers to fluctuate on the physical sites while keeping the total number of particles conserved in the total space (physical and auxiliary).

Remarkably, one can mix the two algorithms and purify only some fermionic sites, creating an hybrid METTS-purification algorithm [14, 15]. The default METTS algorithm discussed above corresponds to purifying no sites. When every site is purified, no METTS sampling is necessary as the purified state computes the density matrix of the whole system. This hybrid algorithm is simple to implement from the original METTS, as the collapse step only needs to be modified slightly: purified sites are ignored at first (not collapsed) and after the collapse on all other sites is completed, purified and ancilla pairs are reinitialized in the maximally entangled state given by Eq. (9) [14].

The choice of the purified sites is a delicate question: it is a free parameter of the algorithm and is certainly model dependent. Two extreme limits are clear. At high temperatures, purifying all of the sites is the most efficient choice. This can be understood by observing that at infinite temperature a full purification immediately gives the exact thermal density matrix without any time evolution or sampling [3]. In contrast, at zero temperature the thermal density matrix is the tensor product $|\psi_0\rangle \langle \psi_0|$ where the ground state $|\psi_0\rangle$ can be represented with a single METTS and thus no purification is needed. Away from these limits, purifying additional sites decreases the amount of sampling that is necessary while increasing the cost of computing each sample. In quantum impurity models, a physically motivated choice is to purify only the sites of the impurity and the bath sites with the largest thermal fluctuations. This approach will be investigated in detail in the next section.

III. APPLICATION TO THE ANDERSON IMPURITY MODEL

A. Model

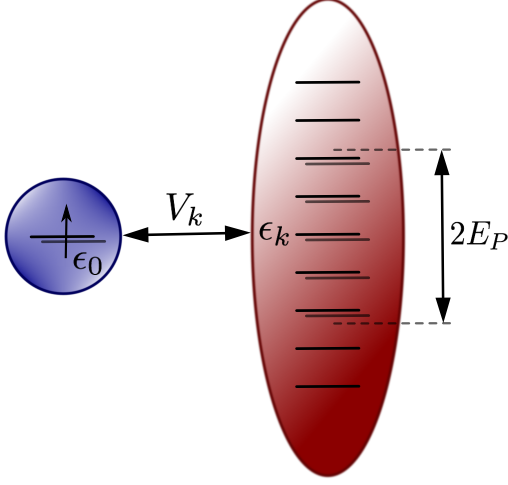


Figure 1. Schematic depiction of the impurity model used in this study. Purified sites are shown as double lines. We choose to always purify the impurity, as well as every bath site with an on-site energy $|\epsilon_k| < E_P$.

We benchmark the hybrid METTS/purification algorithm on a single-band Anderson impurity model, defined by the Hamiltonian:

$$H = U n_{\uparrow} n_{\downarrow} + \epsilon_0 (n_{\uparrow} + n_{\downarrow}) + \sum_{k\sigma} \epsilon_k n_{k\sigma} + V_k (d_{\sigma}^{\dagger} c_{k\sigma} + h.c.) \quad (12)$$

where d_{σ}^{\dagger} and d_{σ} are impurity creation and annihilation operators of impurity electrons with spin σ . The $n_{\sigma} = d_{\sigma}^{\dagger} d_{\sigma}$ are the corresponding particle number operators. Similarly, $c_{k\sigma}^{\dagger}$ and $c_{k\sigma}$ create and annihilate a spin- σ electron at bath orbital k .

In general, the effect of the bath onto the impurity is described by the hybridization function:

$$\Delta(i\omega_n) = \sum_k \frac{V_k^2}{i\omega_n - \epsilon_k} \quad (13)$$

which, in many applications, is a general (causal) function that would require an infinite number of bath sites to represent. Algorithms based on an Hamiltonian representation (like exact diagonalization, DMRG, NRG) require an approximation of Δ by a finite bath in Eq. (12). The precise way to discretize the bath depends on the algorithm in question. Here we use a bath with N_b linearly spaced bath energies ϵ_k [26, 37, 38] (see Appendix A). The energy resolution of our method is given by the difference between consecutive bath energies ϵ_k . In the following, we choose a semi-circular bath of half bandwidth $D = 2$

corresponding to a tight-binding model on a infinite coordination Bethe lattice with hopping parameter $t = 1$. We use $N_b = 109$ sites and we do *not* vary the bath size with β .

B. Algorithm

We apply the algorithm presented in Section II to compute imaginary-time dependent properties of the Anderson impurity model defined above. Before presenting the results, let us discuss aspects of the algorithm implementation which are specific to this system.

First a physically-motivated criterion is needed to choose which sites to purify. Here we choose to purify sites likely to have the largest charge fluctuations, namely the impurity site and bath sites with energy $|\epsilon_k| < E_P$ for some threshold energy E_P , as represented on Fig. 1. It is also natural to purify the impurity itself, because of the Kondo spin flips at low energy.

In order to represent the METTS states, we use the fork tensor product states (FTPS) [37] tensor network, which allows the use of a large number of bath sites ($N_b \sim 100$). The imaginary time evolution is done with the time dependent variational principle (TDVP) [39, 40]. While generally this approach is very accurate even when using large time steps $\Delta\tau$, it can produce incorrect results when bond dimension of the matrix product state is very small as generically happens at the beginning of each step of the METTS algorithm. Therefore, when starting from a product state $|i\rangle$, we first perform a small number of tDMRG [37] (or Trotter-gate evolution) steps to increase the tensor dimensions and then switch to TDVP. In this work, we use a few tDMRG steps of size $\Delta\tau_{tDMRG} = 0.05$. Recently, a basis extension for TDVP was proposed which should allow the use of only TDVP for the time evolution [41]. We however leave this extension for future work.

In practice, we observe that the METTS algorithm revisits the same product states quite often. Depending on E_P and the sample size, 10% – 90% of the METTS appear at least twice. This behavior is quite specific to the quantum impurity problem we study here and the basis used to represent it, and would not be expected to occur in a generic model when working in a real-space basis. Here we can take advantage of it by saving each METTS we have previously computed in memory, reusing them if the same initial product state is encountered, thus skipping redundant imaginary time evolution calculations which are the most costly part of the algorithm.

C. Results

We now present our results for the impurity single-particle Green function (omitting the spin index)

$$G(\tau) = \langle T_{\tau} d(\tau) d^{\dagger} \rangle, \quad (14)$$

which are computed by first performing 20 steps of tDMRG with a time step of $\Delta\tau_{\text{tDMRG}} = 0.05$, and then evolving to $\beta/2$ by TDVP with a time step of $\Delta\tau_{\text{TDVP}} = 0.5$. We use a truncation error cutoff of 10^{-8} for both stages.

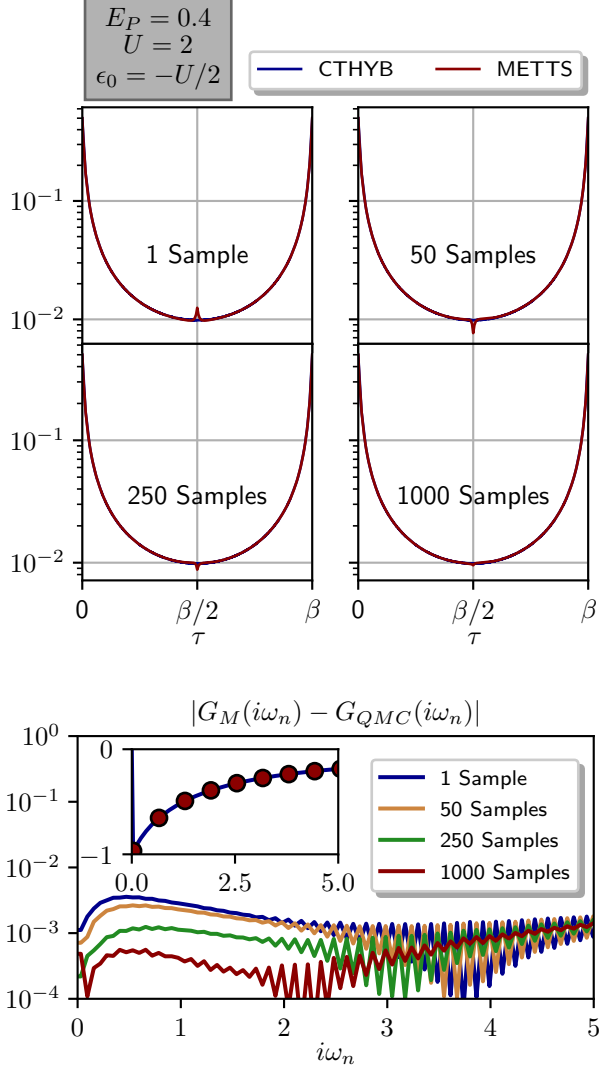


Figure 2. (Upper panel) Imaginary-time Green function $G(\tau)$ vs τ computed by the METTS algorithm for different number of samples, compared to the QMC/CTHYB solution for the same finite discretized bath. For the single-sample panel, we use the highest probability METTS. The fraction of METTS reused was between 0.6 (50 samples, 20 unique METTS were computed) and 0.8 (1000 samples, 200 unique METTS were computed). (Lower panel) Difference between the METTS (G_M) and the QMC result (G_{QMC}). (Inset) METTS (red, with 1000 samples) and QMC results (blue) at low frequencies. For all graphs, we used $U = 2$, $\beta = 100$, $E_P = 0.4$ and $\epsilon_0 = -U/2$ (particle-hole symmetry).

1. Benchmark and convergence

In Fig. 2 we show the Green function, for $U = 2$, at low temperature $\beta = 100$, in the particle-hole-symmetric case, with a purification window energy $E_P = 0.4$. We compare it to a QMC (CTHYB) solution for the exactly the same finite discretized bath, using the TRIQS/CTHYB code [42]. The agreement is excellent even with a small sample size. In Matsubara frequencies (Fig. 2, lower panel), the agreement is also very good even at small frequencies, with an error of order of 10^{-3} . Additional results for larger interactions and particle-hole asymmetric impurity models can be found in Appendix D.

We observe that one of the METTS has a very high probability $P(i)/Z$ and dominates the whole distribution: $P(i)/Z \approx 70\%$ in the present case. Using this state alone (Fig. 2, first panel) already yields an excellent approximation of the Green function. Unsurprisingly, this METTS corresponds to having a filled Fermi sea the set of non-purified bath sites. At this low temperature, purifying about 20% ($E_P = 0.4$) of the bath sites captures most thermal fluctuations already and there is no need to purify every site.

The contribution of other METTS states to $G_i^\pm(\tau)$ are shown in Fig. 3. They display a very large variance around $\beta/2$ (even with sign change). This explains why in Fig. 2 the Green function does not appear to improve when increasing the sample size from 1 to 50. In Figure 9 in Appendix C, we show detailed histograms for $G(\beta/2)$ for various temperatures.

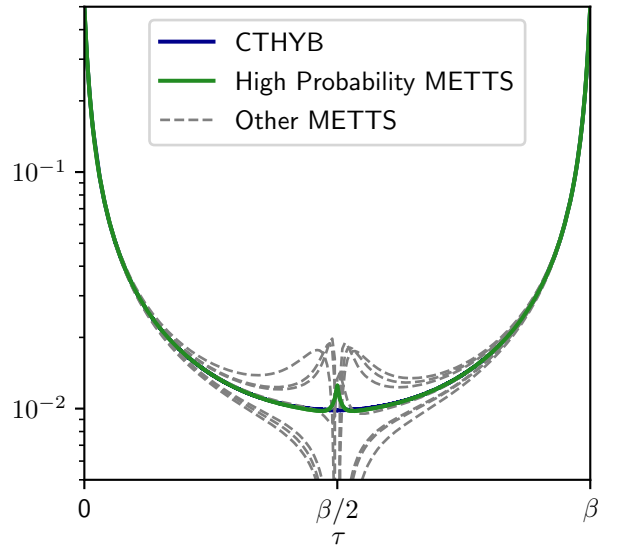


Figure 3. First 8 METTS Green functions in the METTS Markov chain shown in Fig. 2 compared to the CTHYB reference calculation. The highest probability METTS ($P(i)/Z \approx 0.7$) is plotted in green.

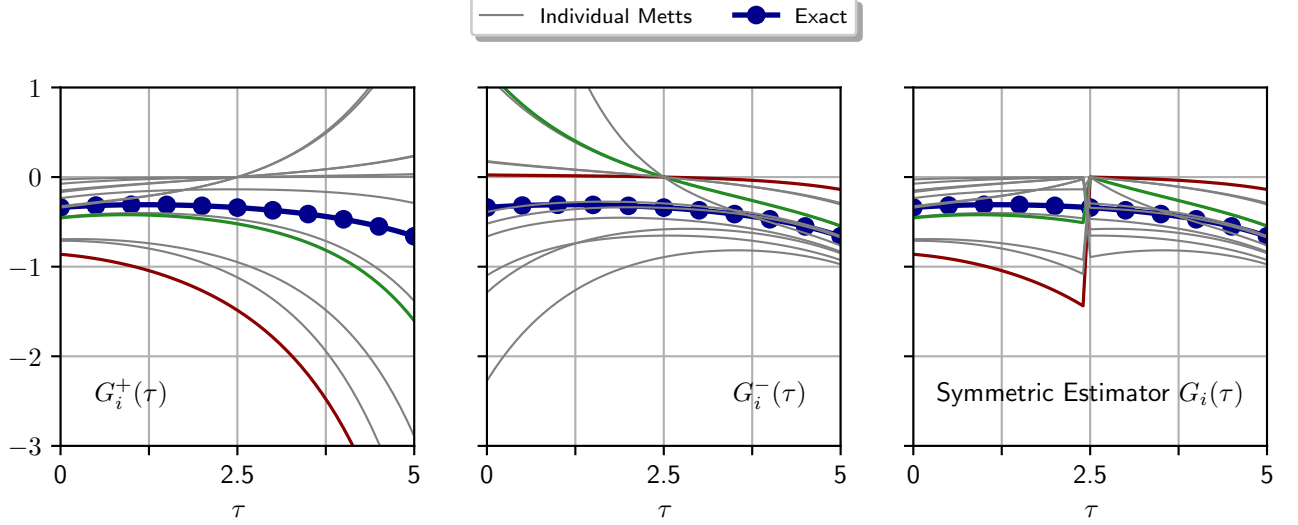


Figure 4. Typical $G_i^+(\tau)$, $G_i^-(\tau)$ and symmetric estimator $G_i(\tau)$ values for a small, non-interacting ($U = 0$) impurity model with seven bath sites at $\beta = 5$. No sites are purified. The plots show the 10 most probable METTS obtained from particle number basis states $|i\rangle$. The exact solution (sum of all METTS) is shown with symbols. Two specific METTS are highlighted in red and green, to show that for the same METTS either $G_i^+(\tau)$ or $G_i^-(\tau)$ can deviate significantly from the average, highlighting the benefit of using the symmetric estimator.

2. Error around $\beta/2$

The error in $G(\tau)$ is mostly concentrated in a relatively small time window around $\beta/2$. It decreases with sampling, but slowly. The reason for that is first, as mentioned above, $G_i^+(\beta/2)$ and $G_i^-(\beta/2)$ differ. This yields a discontinuity in the symmetric estimator, which cancels only on average. Second, the variance of $G(\tau)$ is larger around $\beta/2$ in the sampling.

In order to better understand this phenomenon, we solve a small non-interacting impurity model exactly using a full diagonalization and we do an exact enumeration of all METTS $|\phi\rangle$, without approximation.

The results are presented in Fig. 4, where we plot $G_i^+(\tau)$, $G_i^-(\tau)$ and the symmetric estimator for the 10 METTS with the highest probability $P(i)/Z$. The METTS with the next-highest probability is $P(i)/Z = 0.007$. Both $G_i^+(\tau)$ (resp. $G_i^-(\tau)$) become very large for at least some of the METTS for $\tau > \beta/2$ (resp. $\tau < \beta/2$). As expected, the symmetric estimator Eq. (7) does not become large, but introduces a discontinuity in the contribution from each METTS at $\beta/2$. In both G_i^\pm , the sample variance is greatest around $\beta/2$, as in Fig. 2.

3. Choice of Purification Window

Let us now examine the effect of the purification window energy E_P as a function of β . As discussed above, in this impurity model, a single METTS dominates with a high

probability. The contribution of excitations to the Green function are quite different as shown in Fig. 3. They can even change sign around $\beta/2$. Sampling from such a distribution is clearly hard (see App. C for the shape of the distribution), which is an incentive to increase E_P .

The optimal choice of the purification window energy E_P is therefore a delicate balance. When E_P increases, the computation cost of a METTS increases, but the variance of the distribution decreases. In order to quantify this balance more precisely, we show on Fig. 5 the relative standard deviation (RSD) of $G(\beta/2)$ (left panel) and the computation time per METTS (right panel), for the $U = 0$ case (note that non-interacting models are non-trivial for tensor network approaches). Apart from small β , where it is nearly independent of E_P , the RSD is similar for all β (note however that for large β , $G(\beta/2)$ is very small, so the RSD is large even though the results improve with increasing β). The computing time for a single sample increases with E_P even without taking into account that one would have to actually decrease the truncated weight to get similar accuracies. The difference in computation time between different choices of E_P can be large. For example, a factor of about three can be gained at all values of β if the highest probability METTS of $E_P = 0.4$ is used instead of the full purification.

Finally, we show in Fig. 6 the error of the Green function $G(\tau)$ for various sample sizes, values of β and E_P . Starting from a single sample where we always choose the highest probability METTS, the Green function converges to the exact result by increasing the sample size. Nev-

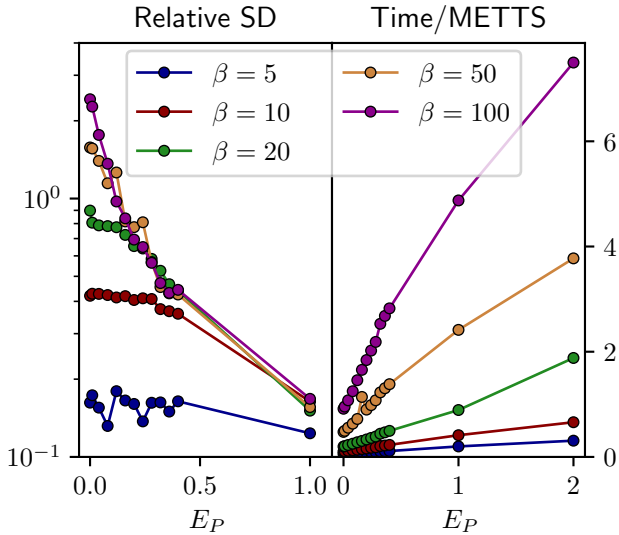


Figure 5. (Left) Relative standard deviation at $\beta/2$ as a function of purification energy scale E_P . (Right) Wall time in (1000s) to compute a single METTS also as a function of E_P . The first two points which are both very close to $E_P = 0$ correspond to only purifying the impurity and purifying the impurity and the zero-energy bath site. Beyond that for $E_P \leq 0.4$, each data point has two additional bath sites purified (one site for positive and negative ϵ_k). Finally note that $E_P = 2$ means that every site is purified and no sampling is necessary at all. Therefore this point is excluded from the plot on the left.

ertheless, in some cases a finite amount of sampling can even result in a worse Green function compared to just using the highest-probability METTS as seen for $\beta = 20$ and $E_P = 1$, for example.

4. Reuse of METTS state

A crucial factor to reduce overall computation times for this class of system is to reuse the already computed METTS. In Fig. 7 we plot the fraction of METTS that appeared at least twice and for which we were able to reuse the Green function and METTS $|\phi_i\rangle$. Like the RSD, this fraction does not strongly depend on β as soon as E_P exceeds some β -dependent value (for $\beta = 10$, $E_P = 0.32$). By purifying half the bath ($E_P = 1$), a β independent fraction of about 90% of the sample can be reused. From these 90%, the by far largest contribution comes of course from the highest probability METTS with a small number $\mathcal{O}(1)$ of single-particle excitations that appear multiple times.

IV. CONCLUSION

We have presented an extension of finite-temperature tensor network algorithms to obtain imaginary-time correlation functions, such as the Matsubara single-particle Green function $G(\tau)$. Though the steps to obtain $G(\tau)$ are straightforward, care is needed in devising estimators with good convergence properties. Benchmarking the algorithm on the single-band Anderson quantum impurity model yields excellent results when compared to well-established quantum Monte Carlo algorithms, with a relative accuracy of order $\sim 10^{-3}$ at low Matsubara frequencies.

For the Anderson model, we purified sites with the lowest magnitude single-site energies while sampling the rest as in the METTS algorithm. One improvement could be to solve the finite-temperature system in the non-interacting limit and purify sites with fractional occupations, rather than using a simple energy criterion. In more general future applications the choice of sites to purify will depend on the specific system. Also the balance between METTS sampling and purification depends on the computing resources available: purifying fewer sites makes each METTS less costly to compute but requires more to be sampled. Yet this sampling overhead can be parallelized away with more nodes available.

An interesting future direction is applying the methods presented here to real space systems, for example lattice models of fermions such as the Hubbard model. METTS and purification already provide accurate results for the strongly-correlated regime of the Hubbard model at low temperatures [43, 44]. Having access to the Matsubara Green function would yield additional insight into phenomena like the metal-insulator transition and Fermi surface properties. In those settings, certain aspects particular to the benchmark impurity system we used here would need to be adapted, especially the choice of which sites to purify.

Another valuable topic to investigate further would be improvements to the algorithm or estimator to enhance convergence near $\tau \approx \beta/2$. Though we still obtained accurate results near this point, it is the slowest to converge due to a discontinuity in the contribution from each METTS as discussed in Section III. Finding an estimator or modified algorithm that would eliminate such discontinuities is an open interesting question.

Finally, the effectiveness of METTS as an imaginary-time solver for more complex, multi-orbital impurity models will be important to investigate. In particular, the optimum balance between purification and METTS could be significantly modified in the multi-orbital case. Nevertheless, since tensor network methods are insensitive to the sign problem which limits usual continuous time quantum Monte Carlo, the algorithm we present here could be a method of choice to solve realistic DMFT equations at low temperatures, especially in the presence of strong spin-orbit coupling.

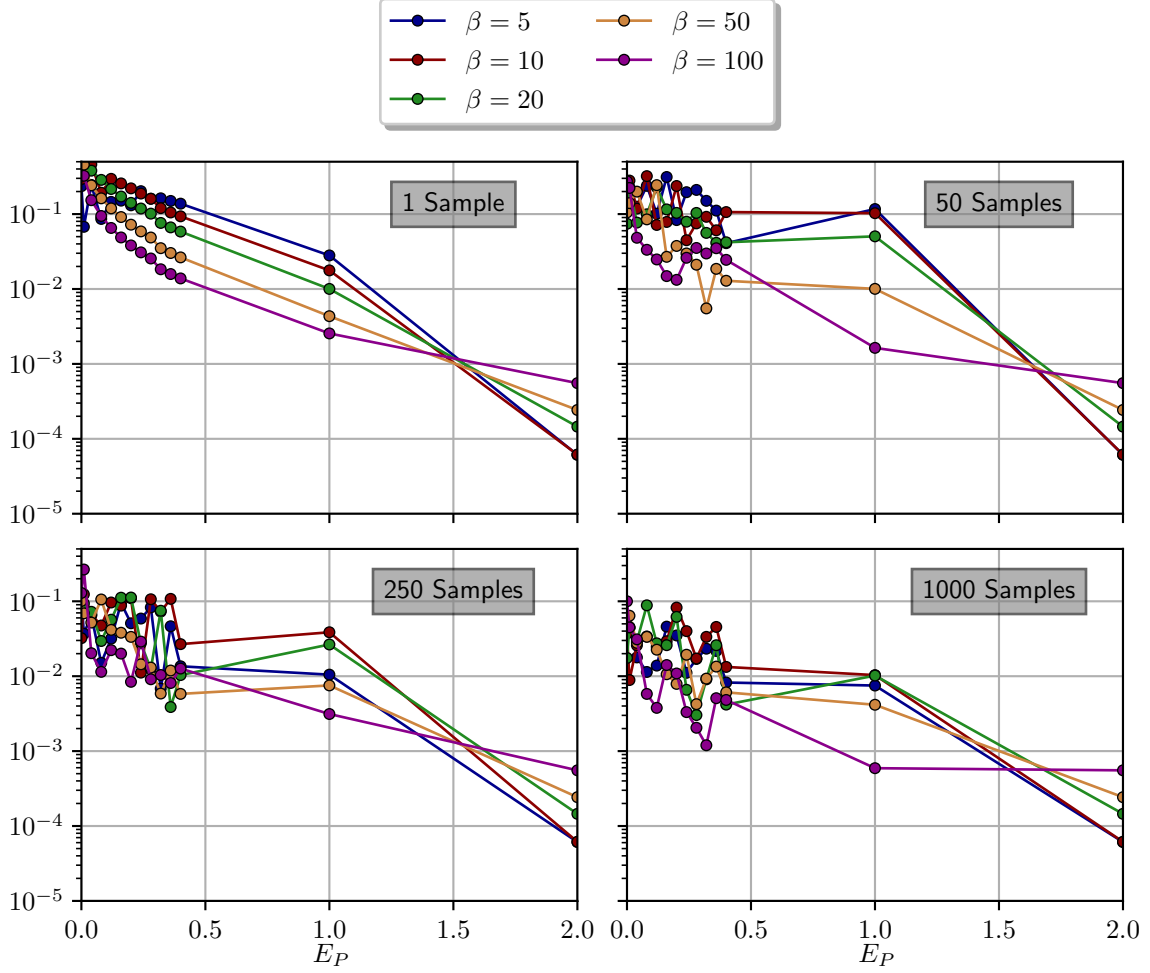


Figure 6. Error defined as $\sum_i |G_{Ex}(\tau_i) - G_{METTS}(\tau_i)|$ for a non-interacting impurity model. For the single sample, we again chose the highest probability METTS. Note that for $\beta = 5$ and low E_P the highest probability METTS is not well defined for the sample sizes studied. Again, the $E_P = 2$ values correspond to the full purification method and for those data points, no sampling is needed.

Appendix A: Bath Discretization

The discretization of the bath starts with a given bath spectral function $-\frac{1}{\pi} \text{Im} \Delta(z = \omega + i0^+)$ (see Eq. (13)). First, we find the energy range $[\omega_L, \omega_U]$ in which the bath spectral function is non-zero. We then split the energy axis into N_b linearly spaced intervals of size $\Delta\epsilon = \frac{\omega_U - \omega_L}{N_b}$ such that the k -th interval $I_k = [\omega_L + (k-1)\Delta\epsilon, \omega_L + k\Delta\epsilon]$. We then place a bath site in the middle of this interval and compute the bath parameters via:

$$V_k^2 = -\frac{1}{\pi} \int_{I_k} d\omega \text{Im} \Delta(\omega)$$

$$\epsilon_k = \omega_L + (k - 0.5)\Delta\epsilon. \quad (\text{A1})$$

Appendix B: Tensor Network

In this appendix we give some additional details about the tensor network itself and the methods used to perform the time evolutions.

The MPS used in this work is depicted in Fig. 8. The impurity degrees of freedom are at the center of the MPS with the spin-up and spin-down bath sorted according to their energy ϵ_k to the left/right of the impurity. The long-range couplings V_k of the Hamiltonian Eq. 12 are no issue for TDVP since the matrix product operator can be computed efficiently with links of dimension 5 only. For tDMRG, we use swap-gates as discussed next.

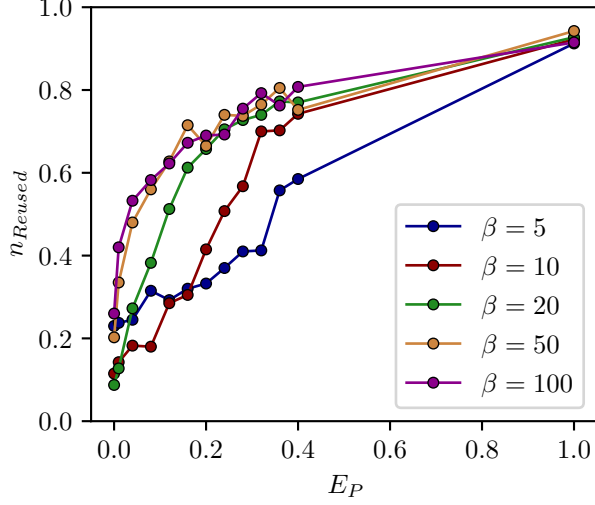


Figure 7. Fraction of METTS reused for a sample of size 400 as a function of E_P . At $E_P = 1$ half the bath sites are purified and a β -independent fraction of about 90% of the METTS appear at least twice. From those, the highest probability METTS is the main contributor followed by the single- and two-particle excitations etc.

tDMRG - Partial Swap Gates

The tDMRG-like time evolution discussed in Ref. [37] uses swap-gates to efficiently encode the long-range hybridization terms of strength V_k . In case we swap a purified site with a normal site, we choose to swap the physical degree of freedom only and keep the auxiliary one untouched, to keep the local degrees of freedom the same size at all times.

We begin with the usual swap gates for fermionic degrees of freedom:

$$S_{dd} = \sum_{n_i, n_j} (-1)^{n_i n_j} |n_i n_j\rangle \langle n_j n_i|,$$

where $|i\rangle$ and $|j\rangle$ are the basis states of the two sites i and j respectively and n_i and n_j are the total occupations. The factor $(-1)^{n_i n_j}$ gives a negative sign if both of the occupations are odd and accounts for the change of fermionic order caused by the swap. These swap gates are used if both Hilbert space dimensions are equal as indicated by the subscript dd , meaning that such a gate is used to swap two normal sites as well as two-purified sites.

To swap a normal site with a purified site, the order in which these two sites appear in the fermionic order matters. The fermionic order on the purified sites is chosen as: $|n_P n_A\rangle = (c_P^\dagger)^{n_P} (c_A^\dagger)^{n_A} |0\rangle$ where P (A) refers to the physical (auxiliary) degree of freedom respectively. So if the normal site comes before the purified site, the swap gate is essentially a generalization of the swap gate

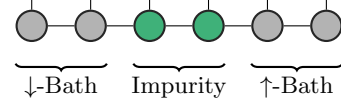


Figure 8. Depiction of the MPS tensor network used to solve impurity models Eq. (12). The physical Hilbert space dimensions of the sites are either 4 if purified or 2 if not purified.

above. The auxiliary site is inactive because it is to the right of the two degrees of freedom being swapped:

$$S_{24} = S_{22} \otimes \mathbb{1},$$

where $\mathbb{1}$ is the 2×2 identity matrix acting on the auxiliary degree of freedom.

If, on the other hand, the normal site comes after the purified site in the fermionic order, the auxiliary site has an effect, because it is in between the two sites being swapped. The resulting swap gate is then given by:

$$S_{42} = \sum_{n_P n_A n_j} (-1)^{n n_j + n_P n_A} |n_P n_A n_j\rangle \langle n_j n_A n_P|,$$

where $n = n_P + n_A$ is the total occupation of the purified site. The sign-factor can be understood as first swapping n_j particles with all n particles on the purified site and then swapping the physical- with the auxiliary degree of freedom of the purified site.

TDVP

The TDVP time evolution is performed with a modified integration scheme compared to the usual right-left-right sweep [39]. Instead, we start the integration in the middle at the impurity, sweep outwards one bath, jump back to the middle and sweep outwards the other bath. Details can be found in the Appendix of Ref [45]. The reason for doing that is two-fold. First, the application of the creation/annihilation operators during the computation of the Green function destroys some tensor network basis states. If we start the time evolution at the sites where this happened allows TDVP to immediately recover the lost bond dimension and reduces the numerical error. The second reason is of practical nature: it is simply easier to generalize to multi-orbital impurity problems, where in the FTPS tensor network, there is no clear left and right anymore.

Appendix C: Green Function Histogram

As mentioned in the main text, the distribution of METTS Green functions is not Gaussian, especially for large values of E_P and around $\beta/2$. Instead, single METTS dominates the distribution and a couple of side bands appear as shown in Fig. 9 (note the logarithmic

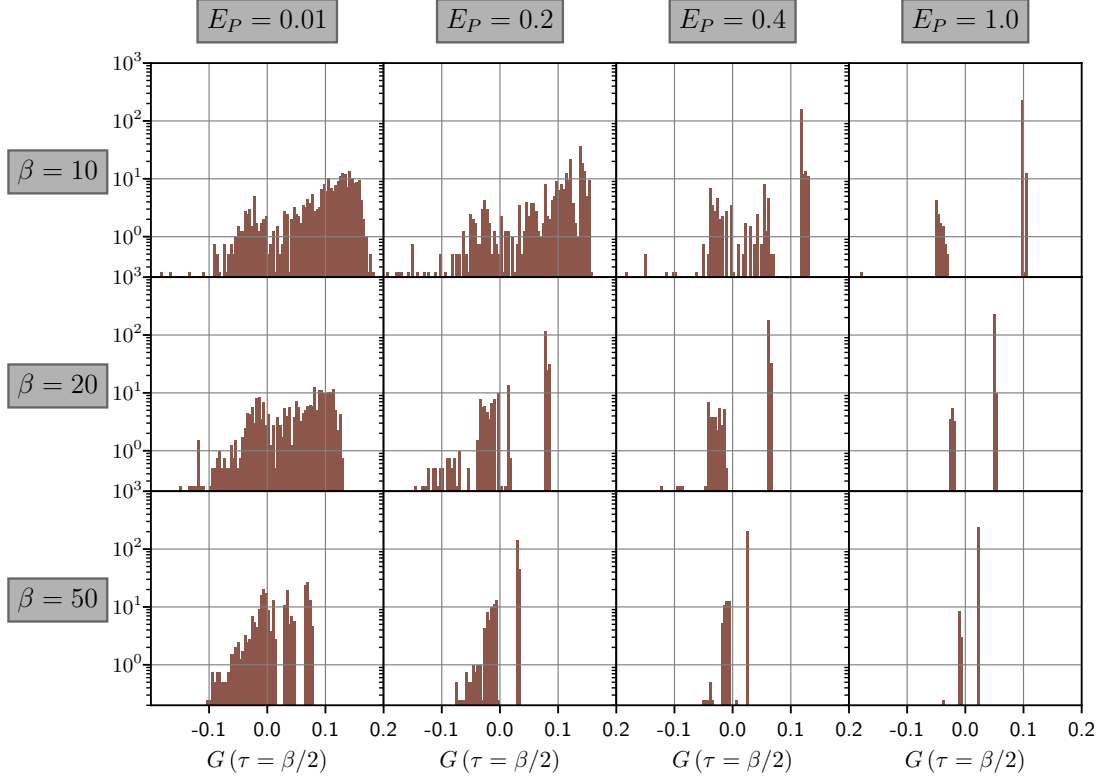


Figure 9. Histogram of single particle Green function at $\tau = \beta/2$ taken from samples of size 1000 at $U = 2$. The left-most column with $E_P = 0.01$ purifies only the impurity and the $\epsilon_k = 0$ bath site. Decreasing β as well as increasing E_P reduces the total width of the histogram. Importantly, with increasing E_P , a single METTS starts to dominate the distribution (called highest probability METTS in the main text).

scale on the y-axis). Even though sampling from such distribution is hard, the highest probability METTS alone often gives a very satisfying result already. Fortunately, in case that computing the highest probability METTS with a sufficiently high E_P is computationally too expensive, decreasing E_P improves the distribution and makes sampling easier.

Appendix D: Additional Results

To obtain a complete picture of the METTS sampling of Impurity Green functions, let us study two additional systems, both in somewhat extreme parameter regions. In Fig. 10, we show Green functions for very strong interactions $U = 8$ and in Fig. 11 for a strongly asymmetric impurity model. Both cases actually perform better than the symmetric $U = 2$ (Fig 2) counterpart with tiny errors even when using just a single sample. This result exemplifies the wide range of applicability of this method with respect to different parameter regimes.

-
- [1] S. R. White, Density matrix formulation for quantum renormalization groups, *Phys. Rev. Lett.* **69**, 2863 (1992).
 - [2] U. Schollwöck, The density-matrix renormalization group, *Rev. Mod. Phys.* **77**, 259 (2005).
 - [3] U. Schollwöck, The density-matrix renormalization group in the age of matrix product states, *Annals of Physics* **326**, 96 (2011), january 2011 Special Issue.
 - [4] S. Paeckel, T. Köhler, A. Swoboda, S. R. Manmana, U. Schollwöck, and C. Hubig, Time-evolution methods for matrix-product states, *Annals of Physics* **411**, 167998 (2019).
 - [5] G. Cohen, E. Gull, D. R. Reichman, and A. J. Millis, Taming the dynamical sign problem in real-time evolution of quantum many-body problems, *Phys. Rev. Lett.* **115**, 266802 (2015).
 - [6] R. E. V. Profumo, C. Groth, L. Messio, O. Parcollet, and X. Waintal, Quantum monte carlo for correlated out-of-equilibrium nanoelectronic devices, *Phys. Rev. B* **91**, 245154 (2015).

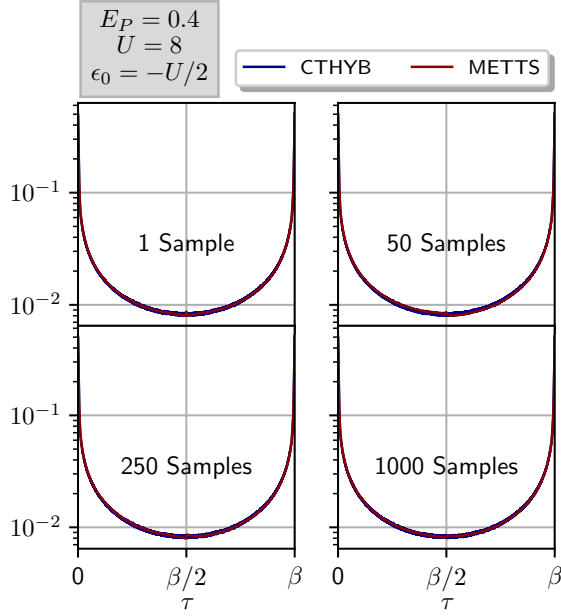


Figure 10. Convergence plot similar to Fig. 2 with very strong interaction $U = 8$ and $\beta = 100$. The result is comparable to its $U = 2$ counterpart and the agreement to CTHYB is even better with nearly negligible errors already for the highest probability METTS.

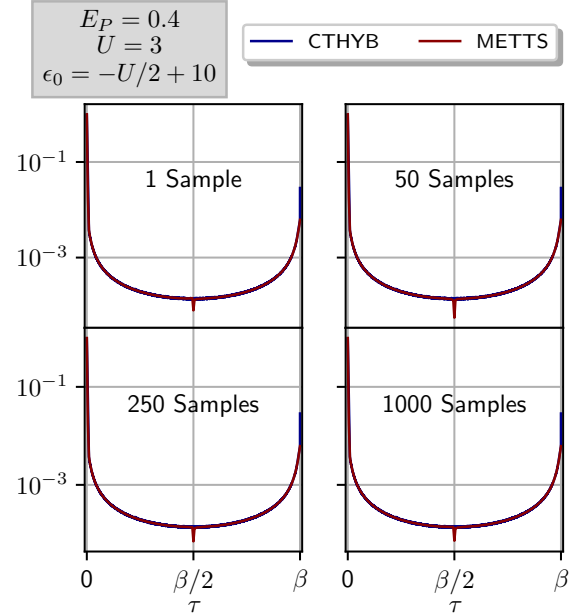


Figure 11. Convergence plot similar to Fig. 2 for a system at $\beta = 100$ with a strongly asymmetric on-site energy $\epsilon_0 = -U/2 + 10$ such that the impurity occupation is only $\langle n_\sigma \rangle \approx 0.006$. Again the agreement is very good especially considering that the Green function at $\beta/2$ is about 2 orders of magnitude smaller than those in Fig. 2 or Fig. 10. The difference exactly at β is attributed to CTHYB sampling problems caused by the low occupation. This means that the METTS result is the correct one at $\tau = \beta$.

- [7] Q. Dong, I. Krivenko, J. Kleinhenz, A. E. Antipov, G. Cohen, and E. Gull, Quantum monte carlo solution of the dynamical mean field equations in real time, *Phys. Rev. B* **96**, 155126 (2017).
- [8] C. Bertrand, S. Florens, O. Parcollet, and X. Waintal, Reconstructing nonequilibrium regimes of quantum many-body systems from the analytical structure of perturbative expansions, *Phys. Rev. X* **9**, 041008 (2019).
- [9] M. Maćek, P. T. Dumitrescu, C. Bertrand, B. Triggs, O. Parcollet, and X. Waintal, Quantum quasi-monte carlo technique for many-body perturbative expansions, *Phys. Rev. Lett.* **125**, 047702 (2020).
- [10] N. V. Prokof'ev and B. V. Svistunov, Polaron problem by diagrammatic quantum monte carlo, *Phys. Rev. Lett.* **81**, 2514 (1998).
- [11] S. R. White, Minimally entangled typical quantum states at finite temperature, *Phys. Rev. Lett.* **102**, 190601 (2009).
- [12] E. M. Stoudenmire and S. R. White, Minimally entangled typical thermal state algorithms, *New Journal of Physics* **12**, 055026 (2010).
- [13] M. Binder and T. Barthel, Symmetric minimally entangled typical thermal states for canonical and grand-canonical ensembles, *Phys. Rev. B* **95**, 195148 (2017).
- [14] J. Chen and E. M. Stoudenmire, Hybrid purification and sampling approach for thermal quantum systems, *Phys. Rev. B* **101**, 195119 (2020).
- [15] C.-M. Chung and U. Schollwöck, Minimally entangled typical thermal states with auxiliary matrix-product-state bases, arxiv (2019), [arXiv:1910.03329 \[cond-mat.str-el\]](https://arxiv.org/abs/1910.03329).
- [16] A. E. Feiguin and S. R. White, Finite-temperature density matrix renormalization using an enlarged hilbert space, *Phys. Rev. B* **72**, 220401 (2005).
- [17] M. Zwolak and G. Vidal, Mixed-state dynamics in one-dimensional quantum lattice systems: A time-dependent superoperator renormalization algorithm, *Phys. Rev. Lett.* **93**, 207205 (2004).
- [18] F. Verstraete, J. J. García-Ripoll, and J. I. Cirac, Matrix product density operators: Simulation of finite-temperature and dissipative systems, *Phys. Rev. Lett.* **93**, 207204 (2004).
- [19] J. Hauschild, E. Leviatan, J. H. Bardarson, E. Altman, M. P. Zaletel, and F. Pollmann, Finding purifications with minimal entanglement, *Phys. Rev. B* **98**, 235163 (2018).
- [20] A. Georges, G. Kotliar, W. Krauth, and M. J. Rozenberg, Dynamical mean-field theory of strongly correlated fermion systems and the limit of infinite dimensions, *Rev. Mod. Phys.* **68**, 13 (1996).
- [21] G. Kotliar, S. Y. Savrasov, K. Haule, V. S. Oudovenko, O. Parcollet, and C. A. Marianetti, Electronic structure calculations with dynamical mean-field theory, *Rev. Mod. Phys.* **78**, 865 (2006).
- [22] A. N. Rubtsov, V. V. Savkin, and A. I. Lichtenstein, Continuous-time quantum monte carlo method for fermions, *Phys. Rev. B* **72**, 035122 (2005).
- [23] P. Werner, A. Comanac, L. de' Medici, M. Troyer, and A. J. Millis, Continuous-time solver for quantum impurity models, *Phys. Rev. Lett.* **97**, 076405 (2006).
- [24] E. Gull, P. Werner, O. Parcollet, and M. Troyer, Continuous-time auxiliary-field monte carlo for quantum

- impurity models, *EPL (Europhysics Letters)* **82**, 57003 (2008).
- [25] E. Gull, A. J. Millis, A. I. Lichtenstein, A. N. Rubtsov, M. Troyer, and P. Werner, Continuous-time monte carlo methods for quantum impurity models, *Rev. Mod. Phys.* **83**, 349 (2011).
- [26] R. Bulla, T. A. Costi, and T. Pruschke, Numerical renormalization group method for quantum impurity systems, *Rev. Mod. Phys.* **80**, 395 (2008).
- [27] K. G. Wilson, The renormalization group: Critical phenomena and the kondo problem, *Rev. Mod. Phys.* **47**, 773 (1975).
- [28] E. Jeckelmann, Dynamical density-matrix renormalization-group method, *Phys. Rev. B* **66**, 045114 (2002).
- [29] D. J. García, K. Hallberg, and M. J. Rozenberg, Dynamical mean field theory with the density matrix renormalization group, *Phys. Rev. Lett.* **93**, 246403 (2004).
- [30] M. Karski, C. Raas, and G. S. Uhrig, Electron spectra close to a metal-to-insulator transition, *Phys. Rev. B* **72**, 113110 (2005).
- [31] K. A. Hallberg, P. Horsch, and G. Martínez, Numerical renormalization-group study of the correlation functions of the antiferromagnetic spin-1/2 heisenberg chain, *Phys. Rev. B* **52**, R719 (1995).
- [32] F. A. Wolf, A. Go, I. P. McCulloch, A. J. Millis, and U. Schollwöck, Imaginary-time matrix product state impurity solver for dynamical mean-field theory, *Phys. Rev. X* **5**, 041032 (2015).
- [33] F. A. Wolf, J. A. Justiniano, I. P. McCulloch, and U. Schollwöck, Spectral functions and time evolution from the chebyshev recursion, *Phys. Rev. B* **91**, 115144 (2015).
- [34] N.-O. Linden, M. Zingl, C. Hubig, O. Parcollet, and U. Schollwöck, Imaginary-time matrix product state impurity solver in a real material calculation: Spin-orbit coupling in Sr_2RuO_4 , *Phys. Rev. B* **101**, 041101 (2020).
- [35] F. A. Wolf, I. P. McCulloch, O. Parcollet, and U. Schollwöck, Chebyshev matrix product state impurity solver for dynamical mean-field theory, *Phys. Rev. B* **90**, 115124 (2014).
- [36] J. Karp, M. Bramberger, M. Grundner, U. Schollwöck, A. J. Millis, and M. Zingl, sr_2mo_4 and sr_2ruo_4 : Disentangling the roles of hund's and van hove physics, *Phys. Rev. Lett.* **125**, 166401 (2020).
- [37] D. Bauernfeind, M. Zingl, R. Triebl, M. Aichhorn, and H. G. Evertz, Fork tensor-product states: Efficient multiorbital real-time dmft solver, *Phys. Rev. X* **7**, 031013 (2017).
- [38] F. A. Wolf, I. P. McCulloch, and U. Schollwöck, Solving nonequilibrium dynamical mean-field theory using matrix product states, *Phys. Rev. B* **90**, 235131 (2014).
- [39] J. Haegeman, C. Lubich, I. Oseledets, B. Vandereycken, and F. Verstraete, Unifying time evolution and optimization with matrix product states, *Phys. Rev. B* **94**, 165116 (2016).
- [40] D. Bauernfeind and M. Aichhorn, Time Dependent Variational Principle for Tree Tensor Networks, *SciPost Phys.* **8**, 24 (2020).
- [41] M. Yang and S. R. White, Time-dependent variational principle with ancillary krylov subspace, *Phys. Rev. B* **102**, 094315 (2020).
- [42] P. Seth, I. Krivenko, M. Ferrero, and O. Parcollet, Triqs/cthyb: A continuous-time quantum monte carlo hybridisation expansion solver for quantum impurity problems, *Computer Physics Communications* **200**, 274–284 (2016).
- [43] A. Wietek, Y.-Y. He, S. R. White, A. Georges, and E. M. Stoudenmire, Stripes, antiferromagnetism, and the pseudogap in the doped hubbard model at finite temperature (2020), [arXiv:2009.10736 \[cond-mat.str-el\]](https://arxiv.org/abs/2009.10736).
- [44] A. Wietek, R. Rossi, F. Šimkovic IV, M. Klett, P. Hansmann, M. Ferrero, E. M. Stoudenmire, T. Schäfer, and A. Georges, Mott insulating states with competing orders in the triangular lattice hubbard model (2021), [arXiv:2102.12904 \[cond-mat.str-el\]](https://arxiv.org/abs/2102.12904).
- [45] C. Bertrand, D. Bauernfeind, P. T. Dumitrescu, M. Maček, X. Waintal, and O. Parcollet, Quantum quasi monte carlo algorithm for out-of-equilibrium green functions at long times, *Phys. Rev. B* **103**, 155104 (2021).